D4

Coupling designs and excitation schemes for single-photon sources

Executive summary

This report summarises the results from tasks 2.2 and 2.3.

Efficient coupling of single-photon emission from a single molecule in a solid-state matrix, namely dibenzoterrylene in anthracene (DBT:AC), into guided modes was investigated. Two approaches were evaluated, yielding estimated coupling efficiencies of ~ 10%. A third approach was partially investigated, with findings suggesting that efficiencies as high as 78% were possible. Finally the design parameters for a fourth approach were obtained in collaboration with the University of Pavia. Measurements of single-photon purity, i.e. $g^{(2)}(0)$, of 0.00 ± 0.03 and indistinguishability of ~ 0.8 were obtained from a DBT:AC nanocrystal located on a gold mirror and surrounded by a solid immersion lens.

Three solid-state quantum dot systems were investigated: optically-pumped InGaAs/GaAs quantum dots emitting in the 930 nm region; a microfabricated monolithic device comprising an electrically-driven LED pumping InGaAs quantum dots emitting in the 935 nm region; optically-pumped InAs/InGaAs/GaAs quantum dots emitting in the 1550 nm region. Measurements were performed for non-resonant, quasi-resonant (p-shell), resonant, and two-photon resonant optical-pumping. In the electrically driven device, the pump LED emission was non-resonant at 785 nm. $g^{(2)}(0) < 0.1$ was observed in all measurements. Two-photon resonant pumping yielded an entanglement fidelity of 0.8 for the optically pumped 930 nm quantum dots and an indistinguishability ~ 0.9 for the 1550 nm quantum dots.

Author list

Benito Alén, Pietro Lombardi, Costanza Toninelli, Sven Rodt, Stephan Reitzenstein, Simone Portalupi, Michael Jetter, Christopher Chunnilall

Contacts

Project Coordinator:	Stefan Kück
Address:	PTB, Bundesallee 100, DE-38116 Braunschweig
Phone:	495315924010
Email:	stefan.kueck@ptb.de

Project website

https://www.siqust.eu/

The EMPIR initiative is co-funded by the European Union's Horizon 2020 research and innovation programme and the EMPIR Participating States

December 2021 v1.0

Table of Contents

Introduction

Single molecules in solid-state matrices were proposed as sources of single-photon Fock states 20 years ago due to their outstanding brightness. Specific guest-host systems, such as the one extensively studied at CNR (i.e. dibenzoterrylene in anthracene, DBT:AC) appear well-suited for integration in hybrid photonic circuits due to: high emission branching ratio in the transition of interest; low refractive index of the host matrix; the possibility of having high-quality emission when embedded in sub-micrometric particles. The challenge to date for integrating molecule-based single-photon sources in photonic chips has been the development of fabrication procedures which maintain the high crystallinity of the host matrix, which is required to guarantee the optical properties of the emitters. Tackling this issue has been the focus of task 2.2.

The aim of the first part of task 2.3 was is to assess the impact of different excitation schemes on the quantum optical properties of single-photon sources. Depending on the excitation scheme, a different density of free carriers will be optically induced and this can lead to spectral diffusion of the quantum dot emission lines. Resonant excitation will be applied to better understand and overcome this issue which is known to limit the degree of indistinguishability. These studies will be performed in the 930 nm and 1550 nm wavelength regions.

The aim of the second part of task 2.3 was to study monolithic devices which can simultaneously drive and tune the emission of single photons by electrical means. Until very recently, electrically-driven single-photon sources have only been based on two-terminal light emitting diodes. In 2017, two groups suggested different designs where two spatially-separated diodes perform the electrical injection and quantum memory manipulation functions independently. Here, the aim was to investigate new multi-terminal devices, testing different designs, reducing their footprint and adding new functionality in terms of tuneability and nanophotonic integration. The targeted monolithic source should be able to emit quantum light when connected to a power supply without the intervention of other light sources. The devices will be monolithically fabricated on semiconductor substrates and could be adapted to different quantum light emitting materials and wavelength ranges; a prototype will initially be demonstrated for single-photon emission around 950 nm and at T < 10 K.

The EMPIR initiative is co-funded by the European Union's Horizon 2020 research and innovation programme and the EMPIR Participating States

1. Single molecules

1.1 Single molecules in solid-state matrices [CNR]

Single molecules in solid-state matrices were proposed as sources of single-photon Fock states 20 years ago due to their outstanding brightness. Specific guest-host systems, such as the one extensively studied at CNR (i.e. dibenzoterrylene in anthracene, DBT:AC) appear well-suited for integration in hybrid photonic circuits due to: high emission branching ratio in the transition of interest; low refractive index of the host matrix; the possibility of having high-quality emission when embedded in sub-micrometric particles [Pazzagli2018]. The challenge to date for integrating molecule-based single-photon sources (SPSs) in photonic chips has been the development of fabrication procedures which maintain the high crystallinity of the host matrix, which is required to guarantee the optical properties of the emitters. Tackling this issue has been the focus of activity A2.2.1.

1.1.1 Integration in waveguides

Materials

Strategies based on three fundamental components have been explored:

1) Molecule-based SPS in the form of nanocrystal (NC) suspension in water;
2) Direct laser writing (DLW) to fabricate polymeric structures;
3) Semiconductor chips with dielectric photonic structures.

As peliminary steps, we have demonstrated:

1) the substantial compatibility of our nanocrystals with the resists used for DLW lithography and polyvinyl alcohol (PVA);
2) a technique for the localized deposition of few NCs based on a micro-infiltration setup that is able to deliver micro-droplet of suspension in predetermined places.

Geometries/Strategies

Four different approaches to reach a scalable platform in which SPSs are efficiently coupled to guided modes were explored. The original plan of the project included two alternative approaches:

<u>Approach #1.</u> Mixing NCs with DLW resists, it is possible to fabricate polymeric structure around preselected molecules.

As a first step, the case of NCs buried in simple waveguides (WGs) was investigated. Due to the proximity of the refractive indices of polymeric resists and glass, the WGs have to be suspended over the substrate in order to hold a strong confinement of the field, as required for high SPS-WG coupling. An arch-like WG with bending radius of 6 μm was designed, with direct coupling to far-field through the glass substrate. Fig. 1 shows a typical device imaged using scanning electron microscopy (SEM).

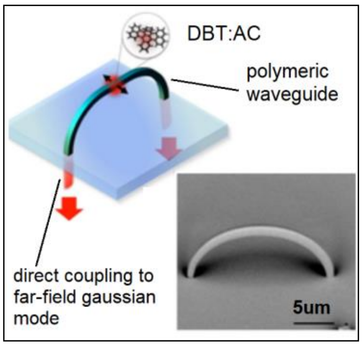

Figure 1. Polymeric fabricated structure

Approach #2. A pre-fabricated ridge WG in Si_3N_4 on SiO_2 with a hole at the centre, terminated with a grating coupler for far-field coupling, was also investigated (Fig. 2). Such a configuration enables the positioning of an NC inside the hole, close to the guided mode field maximum. According to finite-difference time-domain (FDTD) simulations, an enhancement of the coupling efficiency with respect to the case of NC next to a simple ridge WG by a factor 2 is expected.

Localized delivery of few NCs was obtained with the help of a micro-infiltration instrument (Eppendorf FemtoJet).

The selected NC was then protected by a PVA pad fabricated via DLW, while the other nanocrystals are washed out

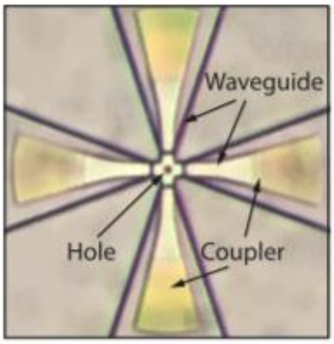

Figure 2. SiN ridge WG with hole

In the second part of the project two other solutions were explored, inspired by the preliminary results with approaches #1 and #2:

Approach #3. Starting from the expertise accumulated working on strategy #2, pre-fabricated dielectric disk resonators were considered, coupled to the far-field with the well-established CNR WG+grating coupler design (Fig. 3).

On one hand, this geometry is more suitable for succesful delivery of few NCs in the useful region by micro-infiltration; on the other, the side the photonic resonances can be exploited to enhance both the emission properties of the molecules and the coupling to the WG mode through the Purcell effect. Disks of 50 μm diameter, which provide a free spectral range on the order of 2 nm, were assessed.

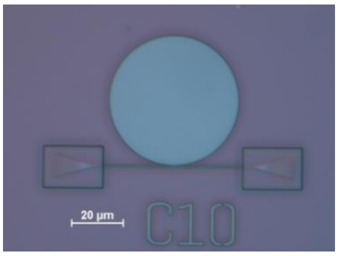

Figure 3. Si_3N_4 disk resonators

Approach #4. As a follow-up to strategy #1, in order to overcome the constraints given by suspended geometries, polymeric ridge WGs fabricated on top of a dielectric Bragg reflector (DBR), were considered (Fig. 4).

In this configuration we can take advantage of the presence of guided modes trapped in the air-dielectric interface, similar to surface plasmon polaritons on metallic surfaces, named Bloch surface waves (BSW). These modes can be conveniently conveyed and spatially localized by shaping an additional layer on top of the multi-layer. With this protocol it is expected to fabricate WGs with propagation losses as low as ~10^{-4} dB/cm [Perani2020].

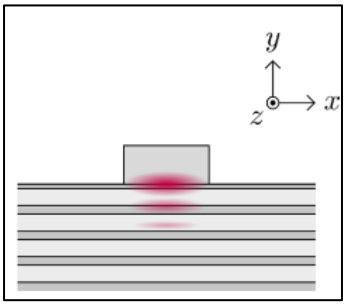

Figure 4. Polymeric BSW WGs

The EMPIR initiative is co-funded by the European Union's Horizon 2020 research and innovation programme and the EMPIR Participating States

1.1.2 Measurements

For each approach the optical characterization of the simple photonic part was first performed. In order to enable a quantitative analysis of signals coming from the guided mode, the couplers‘ far-field efficiency and the input mode matching from free space have to be evaluated.

Coupling efficiencies

For approaches #1 and #2, emitter-WG coupling efficiency for the complete device is reported.

Approach #1: Fully 3D simulations for suspended polymeric WG of 1 μm diameter (as fabricated in the lab) predict an emitter-WG coupling of up to 80%, considering both propagation directions.

The optical properties of the waveguides (Figs. 1 and 5) were experimentally characterized. In figure 5, the light collected from the end-facets corresponds to fluorescence coupled to the guided mode. For typical devices we report: coupler efficiency to far-field ~80%, propagation losses ~13 dB/cm.

Fabrication of the arch WG around pre-selected NCs was possible only for relatively big crystals that are visible with an optical microscope; this has limited the quality of the final device. However we report an additional transmission loss due to the presence of the NC of only ~10%. The emitter-WG coupling efficiency is estimated as ~10% .

Selection of smaller crystals, for which higher coupling efficiency is expected, will be possible by integrating fluorescence imaging capabilities in the DLW workstation. The results are reported in [Colautti2020].

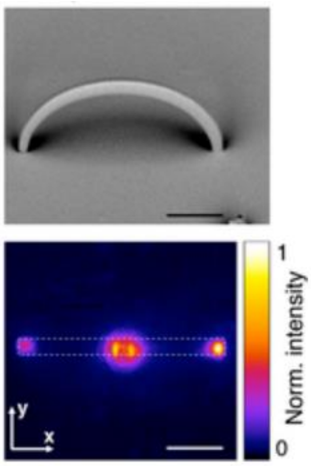

Figure 5. Fluorescence image under confocal illumination of the NC at the center of the WG.

Approach #2: In the central panel (b) of Fig. 6 below the white light image of a device after the whole fabrication procedure is shown: the cross-linked PVA capping pad is evidenced. On the right (c), the fluorescence image upon confocal illumination of the NC inserted in the WG hole for the same device is shown. From this measurement, together with the experimental evaluation of the grating couplers efficiency (~ 25%), and other assumptions based on simulations, an emitter-WG coupling efficiency of around 10% was estimated. The results are reported in [Ciancico2019].

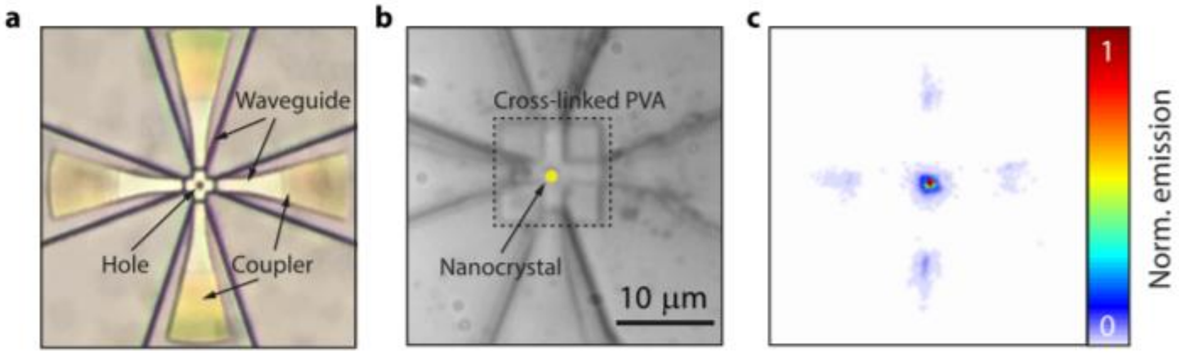

Figure 6. Measurements of SiN ridge WG with hole

2nd-order coherence

Despite the good results obtained in activities A1.3.2 and A3.1.4 concerning photon flux, purity and indistinguishability of the emission from molecule-based SPS in free space, we cannot report measurements for NCs embedded in WGs. In particular, single molecule addressing within the time-scale of the project was not achieved. However, two possible issues in the approaches: the contribution of auto-fluorescence in the polymeric structures to the statistics of the SPS emission, and the effect of DLW on the crystallinity of the host matrix, were investigated. In order to evaluate the relevance of these issues, the ad-hoc structure presented below was investigated. The findings strenghthen the belief that these approaches can be used to achieve the final goal of the project, even if not within the project time scale. We report negligible auto-fluorescence of the polymeric resist, and optical properties for molecules in NCs buried into polymeric structures similar to the onces reported for molecules in bulk samples.

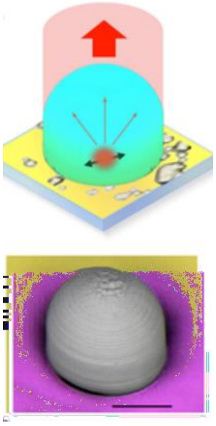

Figure 7. Structure for investigation auto-fluorescence

The structure investigated to determine the auto-fluorescence contribution of the polymeric structure to the statistics of an embedded SPS and the effects of the DLW on its optical properties is presented in Fig. 7. It is constitued by a solid immertion lens fabricated on top of a pre-selected NC. To maximise the collection efficiency, the substrate is a gold mirror, as developed in A1.3.2 . In Fig. 8 below, we report for this device a purity close to unity (a) as measured by the Hanbury Brown and Twiss (HBT) interference measurement of the second-order correlation function $g^{(2)}_{HBT}(\tau)$, an almost Fourier-limited linewidth (b), together with high spectral stability (c), which testify, respectively, to a negligible contribution of auto-fluorescence to the collected photon flux and the full compatibility of the DLW technique and NCs. These results are reported in [Colautti2020].

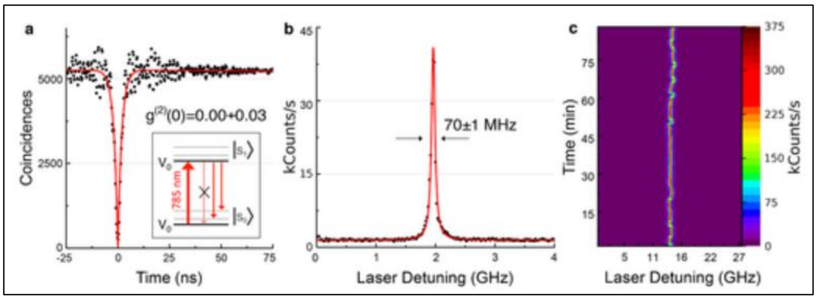

Figure 8. Data obtained from device shown in figure 7.

Indistinguishability

Although not a requirement for this report, the indistinguishability of the emitted photons by single uncoupled molecules under pulsed excitation was measured, yielding visibilities of the order of 80%, which should improve to 95% if the system would be further cooled down to 1.4 K [Lombardi2021].

Preliminary results with approach #3 and #4

Approach #3. In order to estimate the potential of approach #3, the achievable emitter-WG coupling in this configuration was first estimated by combining experimental measurements of Q-factor for real devices and simulations of the EM field spatial distribution for the modes supported by the disks.

The devices‘ optical characterization gives promising results: Fig. 9 shows the transmission spectrum obtained by injecting the WG from the far-field through one grating coupler and collecting light in the far-field from the other coupler, while scanning the frequency of the laser. We report mode Q-factors ~ 10^4-10^5 and a cavity-WG coupling close to optimal for some modes (dips going close to zero transmission).

The spatial distribution of the EM field for low order modes (here reported for the fundamental mode) was then simulated (see Fig. 10), and considering the average Q-factor obtained experimentally, the emitter-WG coupling for different positions of the molecule close to the disk was estimated. A coupling efficiency of up to 78% is expected for molecules in NCs positioned on top of the disk, close to the edge.

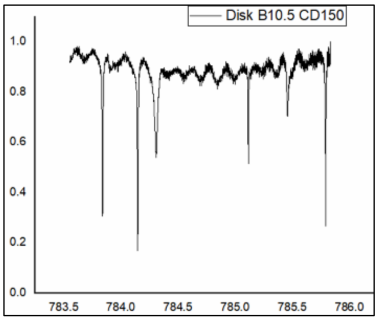

Figure 9. Transmission spectrum

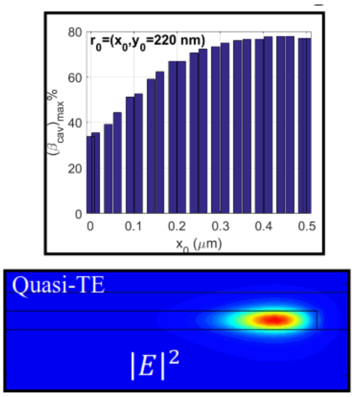

Figure 10. Emitter-WG coupling

The positioning of NCs by means of micro-infiltration was then investigated: on one hand feasibility and yield of the procedure has been tested, on the other hand the effects on Q-factor.

Here we report on the preliminary results for crystal deposition by means of micro-infiltration.

The deposition is suitably localized on the disks, and water surface tension helps positioning close to the edge of the structure (Fig. 11, left image). The presence of fluorescing NCs in useful places after spin-coating of the protective PVA layer has been verified (Fig. 11, centre & right images).

Moderate reduction of Q-factor of the order of ¾ is generally recorded after NC deposition and delocalized PVA capping obtained by spin-coating.

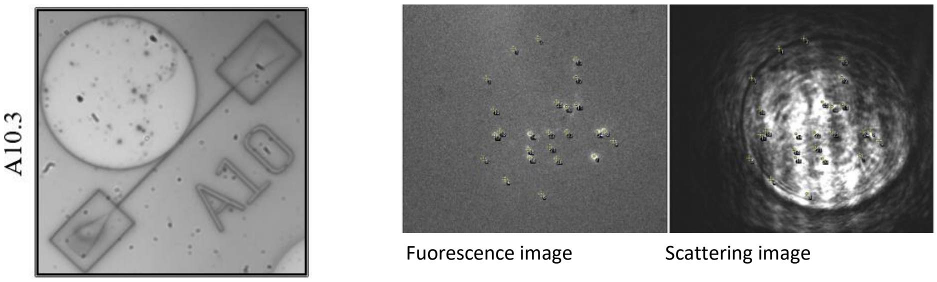

Fuorescence image Scattering image

Figure 11. Disc resonator after NC deposition

Approach #4 - In collaboration with the Liscidini group at the University of Pavia, simulations to determine the multilayer materials and parameters to work with NCs embedded in DLW resist or PVA waveguides was performed. An optimal geometry constituted by SiO_2 and TiO_2 layers was identified (Fig. 11). Losses on the order of 10^{-4} dB/cm are expected for polymeric waveguides 300 nm-thick and 700 nm-wide (Fig. 12).

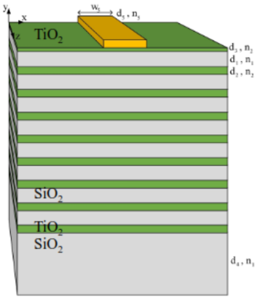

Figure 12. Geometry

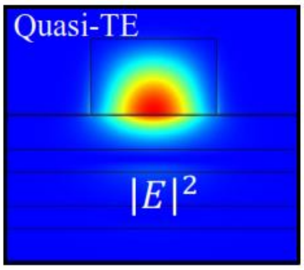

Figure 13. Coupling simulation calculation

The first results related to the fabrication of waveguides for BSW by means of DLW are also reported. A configuration similar to approach #3 (figure 11) was considered for two main reasons:

to enhance coupling efficiency beyond the estimated 40% for a ridge waveguide;

to be able to evaluate the propagation losses and the bending losses regardless the variability of the far-field couplers.

The preliminary stage of fabrication recipe is still being working on and the optical properties of these structures have not been evaluated as yet.

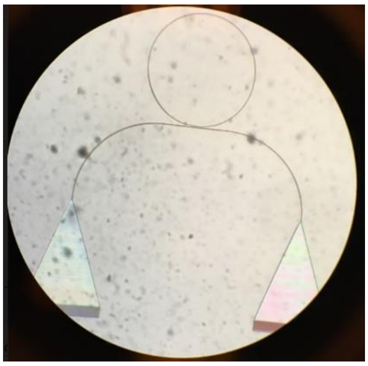

Figure 14. Prototype waveguide geometry

The EMPIR initiative is co-funded by the European Union's Horizon 2020 research and innovation programme and the EMPIR Participating States

2. Quantum dots

Several outstanding results have been achieved by QD-based single-photon sources with high photon extraction efficiency in combination with almost ideal single-photon purity. In order to reach these goals, efforts have been made to develop advanced deterministic nanofabrication platforms and to optimise the optical pumping scheme from the simple non-resonant mechanism to the more challenging and currently more effective resonant excitation.

The aim of the first part of task 2.3 was is to assess the impact of different excitation schemes on the quantum optical properties of single-photon sources. The aim of the second part of task 2.3 was to study monolithic devices which can simultaneously drive and tune the emission of single photons by electrical means. The results from these two tasks are presented below in order of increasing spectral emission wavelength.

2.1 NIR (930 nm region) optically-pumped devices [TUB]

Four different excitation schemes and their impact on the suppression of multi-photon events and the degree of indistinguishability of subsequently emitted photons were investigated for InGaAs/GaAs quantum dots emitting in the near infrared around 930 nm. Amongst them are non-resonant, quasi-resonant, resonant, and two-photon resonant excitation. Additionally, the effect of temporal separation between excitation pulses was evaluated.

2.1.1 Non-resonant excitation

This kind of excitation generates free charge carriers in the bulk material (GaAs) for above bandgap excitation and/or in the InGaAs wetting layer that thermalize into the QDs. This excitation scheme is most easy to realize but there is a high probability that a QD might capture another e-h pair after its initial recombination process and the large amount of free charge carriers leads to dephasing and slight energy shift of excitonic states in QDs via Coulomb interaction. The consequence is an increased probability of multi-photon emission events even under pulsed excitation and the visibility of indistinguishable photons is reduced, too. The latter effect can be reduced by choosing a smaller temporal distance between excitation pulses (e.g. 2 - 4 ns) and by increasing the spontaneous emission rate via light-matter interaction in, e.g., a microcavity by exploiting the Purcell effect. This positive effect of the Purcell effect on the indistinguishability of consecutively emitted photons holds true for the following excitation schemes as well.

2.1.2 Quasi-resonant excitation

Here, the QD is populated with charge carriers via excitation into a higher QD state or by phonon-aided processes. Consequently, there are almost no free charge carriers in its surrounding (at low temperatures) and the diminishing effects from section (2.1.1) are drastically reduced. This is evident from Fig. 15(a) where the FWHM of a trio's emission line under pulsed p-shell excitation is as small as 62 µeV. The corresponding $g^{(2)}(0)$ value for this example equals (12±2)% (Fig. 15(b)).

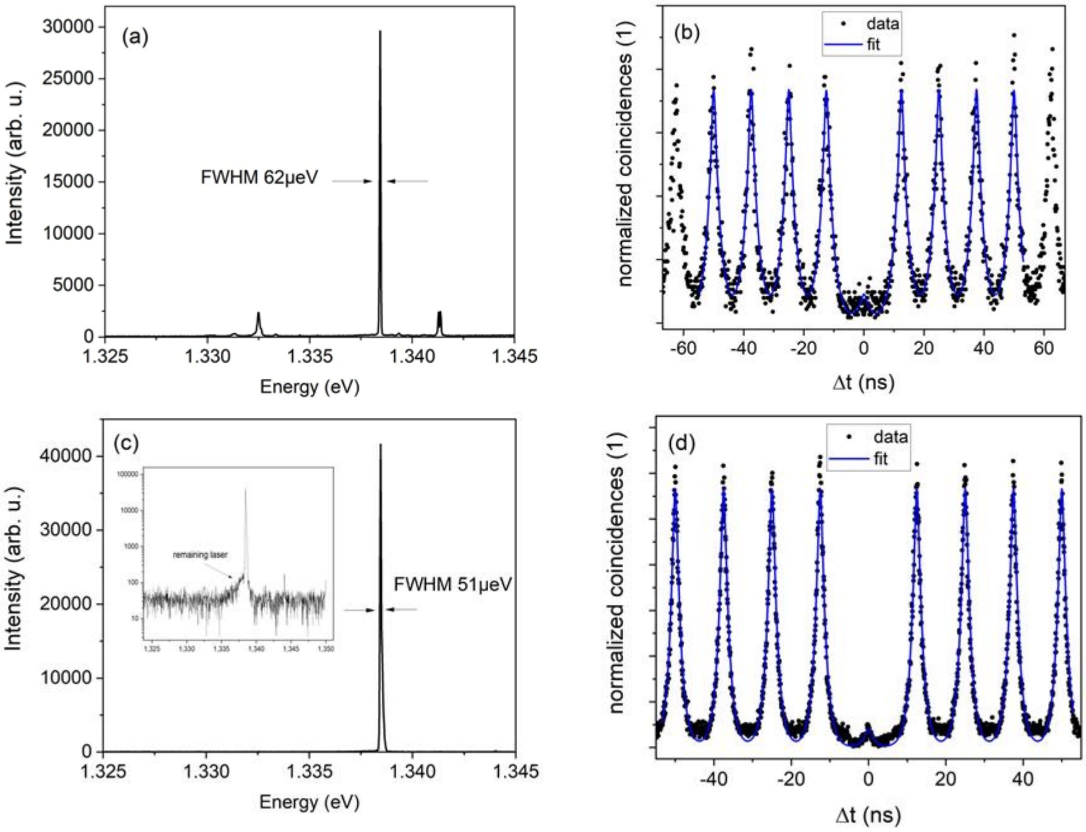

Figure 15. (a) Spectrum of an InGaAs/GaAs QD under pulsed (2 ps length) p-shell excitation in saturation of a trion state at an excitation power of 5 µW. (b) Second order photon autocorrelation measurement (black dots) on the line in (a) and corresponding deconvoluted fit (blue solid line) revealing an antibunching value of $g^{(2)}(0)_{fit,p\text{-}shell}=(12 \pm 2)\%$. (c) Spectrum under pulsed resonant excitation, the inset shows the same data in logarithmic intensity-scaling to make visible the remaining scattered laser. (d) Second order photon autocorrelation measurement on the line in (c) and corresponding fit yielding $g^{(2)}(0)_{fit,s\ shell}=(7.3 \pm 0.5)\%$.

2.1.3 Resonant excitation

Resonant excitation takes place via direct population of the QD's ground state via a resonant light/laser source. However, the resonant photons from the exciting laser overlap spectrally with the

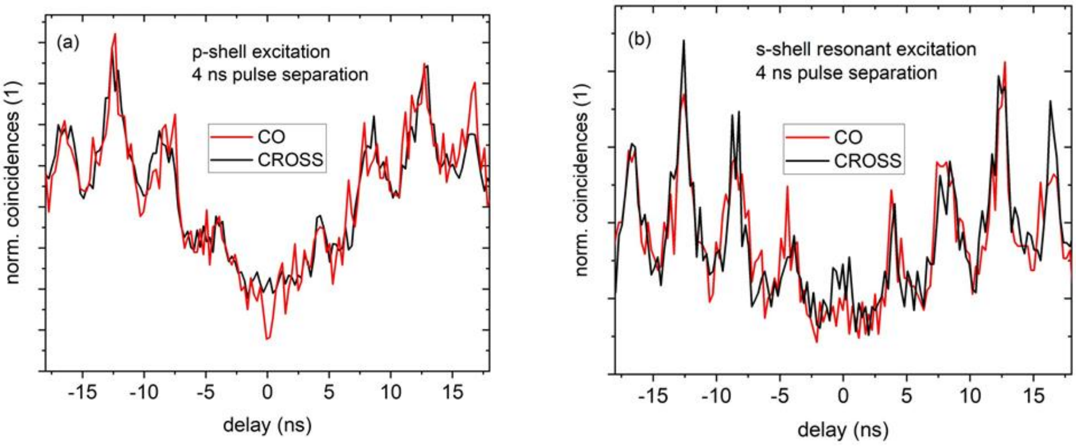

Figure 16. HOM measurements under pulsed excitation with a pulse separation of 4 ns for p-shell excitation (a) and s-shell resonant excitation (b). Although the statistics are rather poor, the positive effect of resonant excitation is obvious around zero time delay.

QD's emission and highly effective stray-light suppression techniques have to be employed to damp the stray light from the excitation source by at least six orders of magnitude. The direct population of the ground state requires no energy relaxation as in the case of p-shell excitation and the quantum optical properties of the emission events are further improved. This is reflected in Fig. 15(c) by a decreased FWHM as compared to Fig. 15(a) down to a value of 51 µeV and in Fig. 15(d) by a $g^{(2)}(0)$ value of (7.3 ± 0.5)%. It must be noted that the present $g^{(2)}(0)$ values are not the best ones and can easily surpassed by non-resonant experiments on high-quality emitters, but the general trend of enhancing the emission properties and quantum nature of emission by more resonant excitation is clearly demonstrated for one and the same QD. The same holds for the generation of indistinguishable photons which is shown in Fig. 16 for one and the same QD.

2.1.4 Two-photon resonant excitation

This kind of excitation is possible only for, e.g., the biexciton state, as momentum conservation requires the generation of, e.g., two excitons. Nevertheless, here it is very efficient and thanks to the biexciton binding energy, the laser energy is shifted with respect to the biexciton and exciton emission energies (Fig. 17) and can easily be filtered out. We were able to demonstrate a biexciton-exciton polarization entanglement of 80% [Bounouar2018]. This kind of resonant excitation also allows for autocorrelation measurements that are not diminished by the laser's stray light. This is demonstrated in Fig. 18 by a CW autocorrelation trace for an excitonic transition under two-photon resonant excitation.

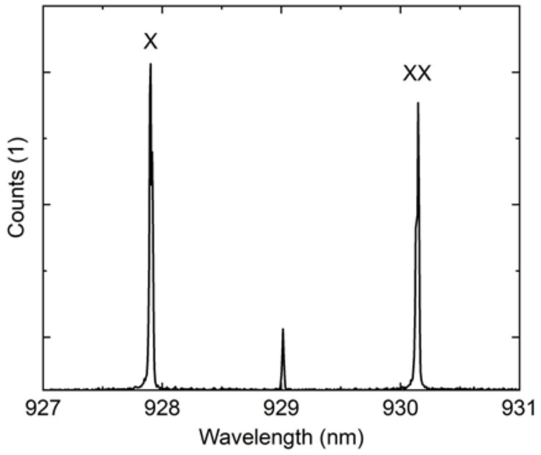

Figure 17. Demonstration of the population of the biexciton state via two-photon resonant excitation with emission from the biexciton and exciton. Thanks to the biexciton binding energy, the laser energy is shifted with respect to exciton and biexciton emission.

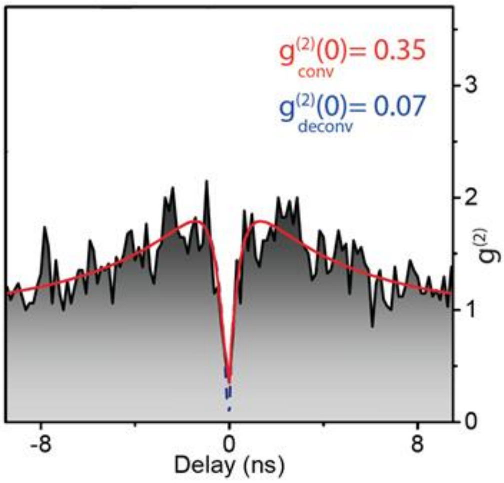

Figure 18. Autocorrelation measurement for an excitonic transition under cw two-photon excitation. Bunching on a longer time scale can be attributed to blinking of the emitter. The deconvoluted $g^{(2)}(0)$ value amount to 0.07.

2.2 NIR (935 nm region) electrically-driven devices [CSIC]

From the point of view of the excitation, most of the reported SPSs rely on optical excitation, since the number of electrically driven sources are more scarce. Since the seminal experimental realization of such a quantum light emitting diode [Yuan2002], different groups have achieved high operation rates. Direct injection in a p-n diode structure was indeed very promising although it also presented two main limitations: firstly, it is difficult to get independent control of the single-photon rate and wavelength since both depend of the current flowing through the diode; secondly, direct current driving of the quantum emitter is inefficient when the current must flow through a nanopatterned structure as required in a nanophotonic environment.

Within SIQUST, how to overcome these difficulties by using hybrid electro-optical pumping schemes in a monolithic device has been explored. The resulting device design has been patent protected during the project and comprises two light-emitting diodes (LEDs) fabricated back to back in a single epitaxial step [Alen2019a]. At the bottom of the device, the master LED is forward biased and emits classical electroluminescence towards the slave LED sitting on top. InGaAs quantum dots (QD) embedded in the slave LED absorb this classical light and emit quantum light (single photons). Tunability can be achieved via the Stark effect by applying a DC voltage at the contacts of the slave LED [Alen2018, 2019b, 2020]. Several epitaxial and device layout designs have been fabricated and characterized resulting in two fully functional prototypes.

In addition, single photon extraction optimization has been explored by designing a novel nanophotonic structure adapted to our excitation scheme which confines most of the QD emission in a narrow cone of NA = 0.17 while reducing the QD emission lifetime by the Purcell effect.

Materials

All devices fabricated so far are based on AlGaAs/GaAs heterostructures containing GaAs Quantum Wells (QW) as pumping material and InGaAs QD to produce single photons around 935 nm.

Electronic design

This task comprised the design of an optimized epitaxial layout through FDTD, transfer matrix and self-consistent Schrödinger-Poisson solver methods.

PNP bipolar junction transistor (BJT) structures and PN-Schottky device layouts have been considered. Galvanic isolation between the master and slave diode is required to avoid QD charging and thus the central doped region (base contact) was optimized to exhaust the majority carrier injection under forward bias of the master diode.

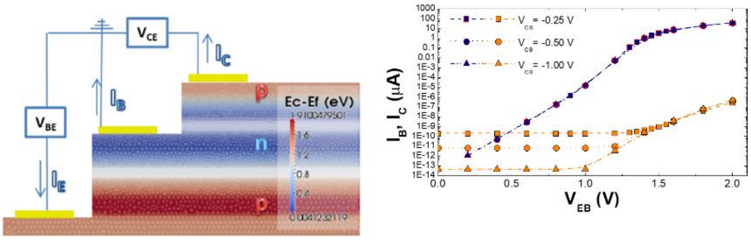

Figure 18. Left: Energy band gap variation at zero bias; Right: Forward Gummel plot of the simulated pnp structure.

Epitaxial Growth

During the project, two 3‘‘ wafer epitaxies were produced containing the full device structure. The growth condtions for the different layers were optimized through several epitaxial/characterization rounds. The optimized epitaxial structures contain low density QDs with emission centred at 930/940 nm, respectively. GaAs/AlGaAs multi-QW emission is centered around 780 ± 3 nm. In between, luminescence from the GaAs p-regions can be observed.

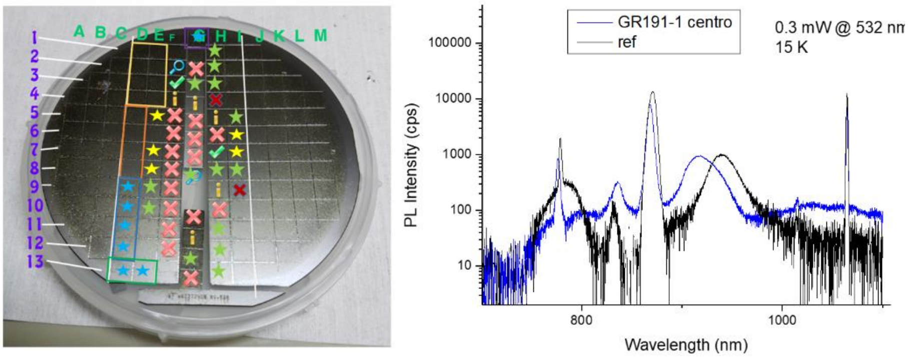

Figure 19. Left: 3 inches wafer diced into 5x5 mm chips; Right: Ensemble photoluminescence of the final epitaxial structures (measured at 10 K with excitation at 532 nm)

Device Fabrication

During the project a microfabrication custom recipe combining UV lithography, wet etching and metal and dielectric deposition was developed. The fabricated devices had varying dimensions, shapes and electrical contacts depending on the device generation.

Generation #1 and #1rev was used to explore possible device geometries and sizes. Each 5 mm x 5 mm chip contained 112 individual devices with diameters of the slave diode mesa ranging between 10 - 50 µm. Around ten chips were fully electrically characterized at room temperature. One chip from each generation was encapsulated and investigated at 4 K by confocal microspectroscopy. Optimization of the etching was critical at this stage to produce a reliable electrical contact metallization over the mesa vertical walls.

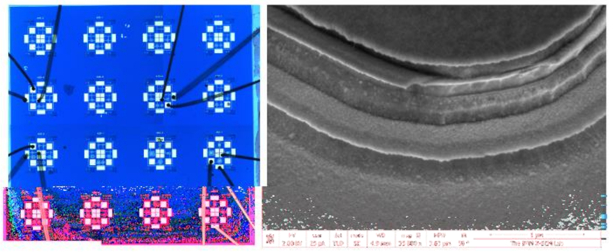

Figure 20. Generation #G1 and #G1rev. Left: 5 mm x 5 mm chip containing 112 devices; Right: SEM image of an unoptimized etching from G1

Generation #G2 was completely redesigned selecting a single device layout geometry and size. The number of devices per chip was reduced to 18 increasing the area for contact pads. The chips were packaged on commercial LTCC DIL16 (low temperature co-fired ceramics, dual-in-line) packages. These changes resulted in 80 % fabrication yield and much beter robustness and reproducibility of the packaging.

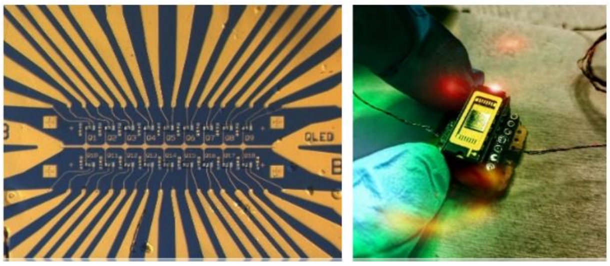

Figure 21. Generation #G2. Left: 5 mm x 5 mm chip containing 18 optimized devices; Right: DIL16 chip carrier used for low temperature measurements.

Five chips were fabricated on pnp and pn-Schottky epitaxial structures and fully electrically characterized at RT. Selected devices were encapsulated and investigated at 4K by confocal micro-spectroscopy.

Electrical Measurements

DC I/V characteristics of each fabricated device were measured at RT in a three-terminal probe station.

The forward Gummel plot, Fig. 23, in common base configuration reflects the electrical coupling between master and slave diodes through majority carrier injection across the base contact. Contrarily to a BJT transistor, for our application this coupling needs to be minimized. In our epitaxial structures, an attenuation factor of 33 dB was typically achieved

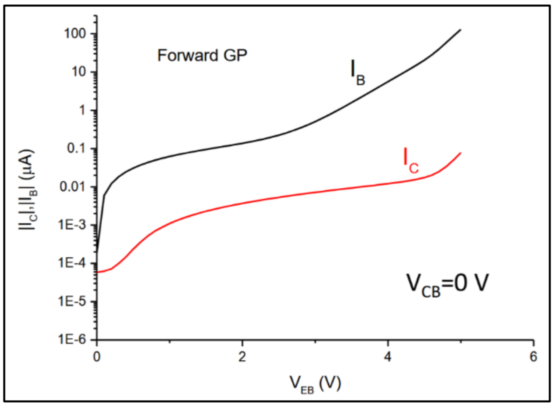

Figure 22. Forward Gummel Plot of fabricated device

Confocal Microspectroscopy Measurements

Selected devices were investigated at 4 K using a confocal imaging microscope and high resolution spectrometers. Once the optimal conditions were set, the single photon purity and first lens rate were determined with SPAD modules in a HBT interferometry setup. By the end of the project, an attempt was made at TUB, to characterize the indistinguishability of the single photon source by HOM interferometry. The single-photon count rate on the measured devices was a factor 10 lower than expected and is currently under investigation.

The images in Fig. 24 reflect the working principle of the device. On the left panel, the emission at 785 nm results from electroluminescence (EL) generated by 100 µA injected into the master diode. The blue region delimitates the slave diode top mesa. This EL is absorbed and re-emitted as wetting layer luminescence at 870 nm (middle panel) and single QD luminescence at 940 nm (right panel).

The InGaAs self-assembled QDs embedded in the slave diode have state-of-the-art properties. In Fig. 25, the observed FWHM = 35.4 µeV was limited by the spectrometer resolution. Fine structure splittings around 40 µeV and exciton lifetime around 800 ps were typical. 30 µm x 30 µm confocal microscopy images measured at 4 K. Observed exciton spectrum

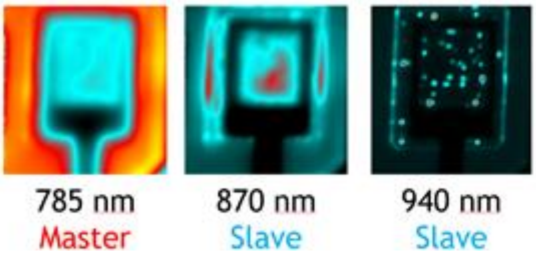

785 nm Master | 870 nm Slave | 940 nm Slave

Figure 23. 30 µm x 30 µm confocal microscopy images of device measured at 4 K.

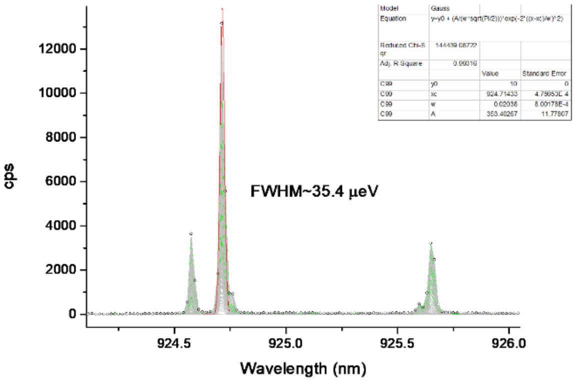

Model	Gauss		
Equation	y=y0 + (A/(w*sqrt(PI/2)))*exp(-2*((x-xc)/w)^2)		
Reduced Chi-Sqr	144439.08722		
Adj. R-Square	0.99016		
		Value	Standard Error
C99	y0	10	0
C99	xc	924.71433	4.75953E-4
C99	w	0.02038	8.00178E-4
C99	A	353.40267	11.77807

Figure 24. Observed exciton spectrum.

The EMPIR initiative is co-funded by the European Union's Horizon 2020 research and innovation programme and the EMPIR Participating States

In Fig. 26, the emission rate of different exciton complexes from the same QD are shown as a function of the master diode injected current, I_{MASTER}. Full saturation is achieved for $I_{MASTER} < 70$ µA corresponding to a first lens single-photon rate of 530 kHz. Below saturation, HBT interferometry was performed revealing a $g^2(0) < 0.1$.

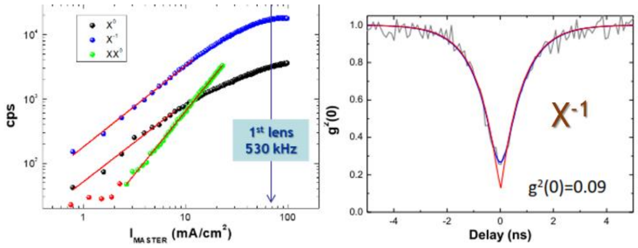

Figure 25. Left: Exciton emission rate vs master current; Right: Single photon purity

Key to our design is the possibility to tune independently the single-photon emission rate and wavelength. This is achieved by varying the master diode current and slave diode voltage, respectively (Fig. 27). While the epitaxial structure can still be improved for better functionality, such a crucial result was demonstrated in two different device prototypes (pnp and pn-Schottky).

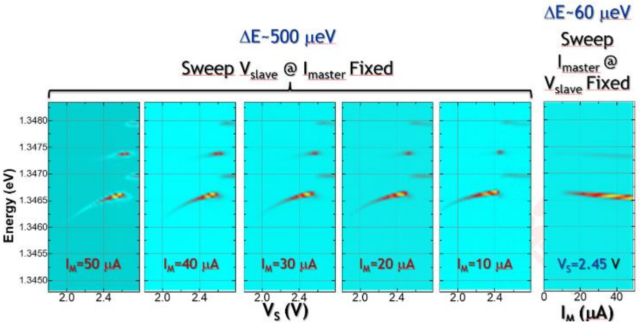

Figure 26. Independent control of emission rate and wavelength

Nanophotonic design for improved single photon extraction/coupling

A custom microphotonic structure to boost the single-photon rate and its coupling to single-mode fibres in the future was designed. The device works on its own without the need for an external excitation laser. The front surface can instead be used to arrange gold contacts which serve both as electrical gates and optical mirrors. In this configuration, single photons are extracted through the substrate side.

The design comprises a micropillar structure located between a top metal contact and a semi-transparent Bragg reflector. Both structures create a vertical optical cavity where Tamm modes and surface plasmon modes are intertwined with Mie resonances provided by the lateral dielectric confinement. An analysis of the structure performance has been done for QDs located at different heights and emitting around 940 nm. For the optimized case, the out-coupled single-photon rate could reach 3 GHz in a narrow cone of NA = 0.17 through the substrate side.

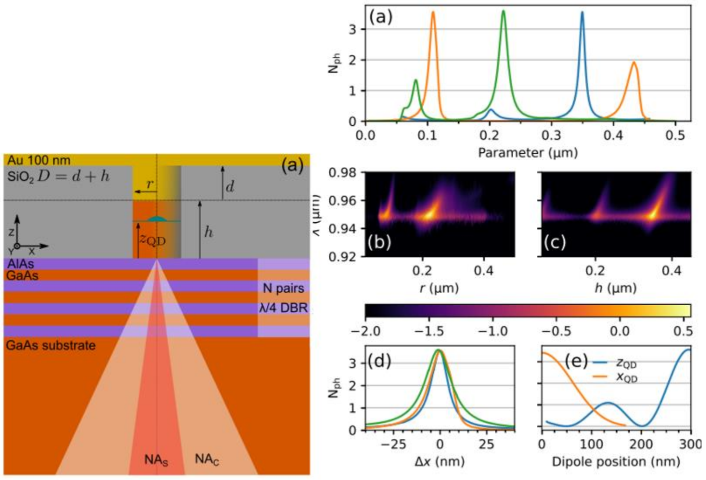

Figure 27. Left: microphotonics structure; Right: performance analysis

2.3 Telecom wavelength (1550 nm region) implementation [USTUTT]

The impact of different pumping schemes on the QD properties and on the emission performances has been investigated. The effect on the linewidth, and hence the photon coherence, under different excitation mechanisms, is first discussed. The single-photon emission and photon indistinguishability under CW two-photon excitation, quasi-resonant p-shell pumping and purely resonant excitation is then reported.

The coherence properties of photons emitted in the telecom C-band from InAs QDs on an InGaAs metamorphic buffer (MMB) based on a GaAs substrate are reported. Below the MMB, 20 distributed Bragg reflector pairs consisting of AlAs/GaAs are used to increase the brightness of the sample. As a measure of the coherence, the linewidth of the emission was investigated for excitation of the charge carriers above the band gap of the barrier material (above-band), via the phonon sideband (phonon-assisted) and in resonance fluorescence (RF). Furthermore, different measurement techniques for the linewidth are compared. The coherence of photons can be characterized by the coherence time T_2 or its inverse, the linewidth Γ_{FWHM}, and in analogy to nuclear magnetic resonance is described by $\Gamma_{FWHM} = 1/T_2 = 1/(2T_1) + 1/T_2^*$, where T_1 stands for the radiative lifetime and T_2^* is referred to as the elastic or pure dephasing time. The first term leads to a homogeneous broadening and a Lorentzian spectral line shape. The latter includes broadening effects due to an unstable electrical and magnetic environment resulting in a Gaussian contribution to the lineshape. While the first term can be changed via the Purcell effect, the latter depends, amongst others, crucially on the excitation scheme of the QD. In general, both broadening mechanisms are present and the spectral lineshape results in a Voigt profile, in principle allowing access to both the homogeneous and the inhomogeneous contribution. The decay time is determined via time-correlated single photon correlation (TCSPC) measurements on 12 exemplary QDs yielding a value for Γ_{FWHM} of 0.3 GHz. However, due to possibly present non-radiative recombination channels, the decay time is generally smaller than the radiative lifetime leading to an overestimation of the linewidth as given here. For a direct evaluation of the spectrum, a grating spectrometer with a resolution of ~40 µeV (or 11 GHz) at 1550 nm is used. When excited above the band gap of the barrier material, the charge carriers relax down to the discrete QD states via the emission of phonons. This interaction is detrimental for the coherence resulting in a large linewidth taken as the FWHM of the Voigt profile. For 14 exemplary QDs this yields an average linewidth of 12.3 GHz with a standard deviation of 2.6 GHz. An exemplary spectrum with such a fit can be seen in Fig. 29(a).

Due to the limited resolution, the homogeneous and inhomogeneous contributions to the linewidth cannot be reliably determined in this way. To circumvent this problem, the coherence is evaluated in the temporal domain by using a Michelson interferometer with a travel range of 150 mm. For the case that both broadening mechanisms are present, the interference visibility as a function of time delay due to asymmetry of the interferometer arms, i.e. the first-order coherence function, is fitted with the Fourier transform of a Voigt profile, i.e. a Gaussian multiplied with an exponential decay. This type of measurement on the same QD as in Fig. 29(a) is depicted in Fig. 29(b). On average, this evaluation yields a FWHM that is 1.6 GHz smaller than its counterpart evaluated in the spectral domain, owing most probably to the limited spectrometer resolution.

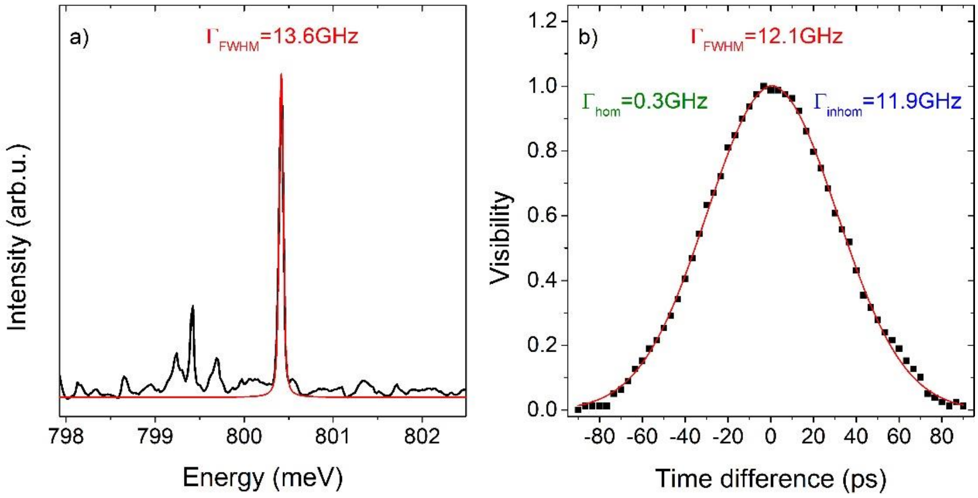

Figure 28. Measurements of the linewidth in above-band pumping. a) Microphotoluminescence spectrum with a Voigt fit and the resulting FWHM. b) First-order coherence function. The red line is a fit using the Fourier transform of a Voigt profile with the calculated linewidth (contributions).

In the temporal domain the homogeneous (inhomogeneous) contribution Γ_{hom} (Γ_{inhom}) can be evaluated yielding an average homogeneous linewidth below 1 GHz meaning that in above-band pumping more than 90% of the linewidth is due to inhomogeneous broadening mechanisms. This measurement technique however is also limited in resolution, as can be seen by a discrepancy of 0.6 GHz between the homogeneous linewidth and the Fourier-limited linewidth expected from the TCSPC measurements. Furthermore, a higher brightness is required for the evaluation with the Michelson interferometer. To decrease the overall linewidth, the charge carriers can also be excited via the phonon-sideband. Due to the limited brightness the coherence is only evaluated in the spectral domain, yielding a decrease of 2.2 GHz in the average linewidth. Some of the emission lines, however, are resolution-limited so this value is most likely an underestimation of the decrease in linewidth. The most favourable pumping scheme in terms of coherence properties is RF. To evaluate the lineshape, the laser frequency is scanned over the resonance of interest and the integrated intensity is recorded, as depicted for an exemplary QD in Fig. 30.

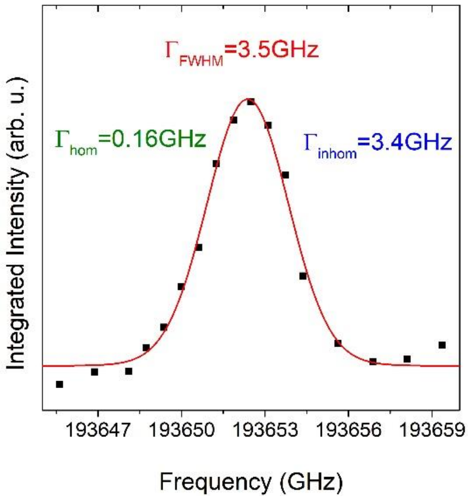

Figure 29. Resonant scan of the excitation laser over the emission line displaying the integrated intensity over the laser frequency alongside a Voigt fit with the numerical value of the FWHM. The central frequency corresponds to a wavelength of 1548.1 nm.

This was done for 5 QDs yielding a FWHM of 3.5 GHz and therefore a further decrease of 6.6 GHz when compared to phonon-assisted pumping. The homogeneous contribution to the linewidth yields an average of 0.35 GHz and is in good agreement with the value expected from the TCSPC measurement. The inhomogeneous broadening mechanisms still account for more than 90% of the overall linewidth. A reduction of these processes could be achieved via a stabilization of the electronic and magnetic environment of the QDs via e.g. a weak off-resonant laser exciting enough charge carriers to fill the charge carrier trap states in the surroundings of the QD, or by applying a magnetic field, respectively. In summary, a systematic study on the coherence properties of InAs QDs on a GaAs basis emitting in the telecom C-band has been conducted. Regarding the measurement methods, the limited spectral resolution of a spectrometer can be overcome by employing a Michelson interferometer. This, however, requires sufficient brightness and a longer measurement time. The ability to scan the laser frequency over the QD resonance, while only possible for RF using a precisely tuneable laser, yields reliable information on the linewidth. Another possibility would be to employ a scanning Fabry-Pérot interferometer. Concerning the excitation schemes, switching from above-band to phonon-assisted excitation reduces the FWHM of the emission lines on average from 12.3 GHz to 10.1 GHz, while a resonant excitation yields average values as low as 3.5 GHz, clearly distinguishing it as the most promising for applications requiring a high degree of coherence, such as two-photon interference.

Combining the advantage of resonant state preparation and the possibility of deterministically preparing the radiative decay via the XX-X cascade, two-photon excitation has been identified as an appealing way of excitation (the following TPE results are taken from [Nawrath2019]). The energy scheme and the corresponding spectrum are shown in Fig. 31(a); the laser (green) and symmetrically equidistant peaks stemming from the X and XX states (blue and dark red) can be seen. The same integrated intensity of these lines is a first footprint of TPE. The spectral feature around 1552.5 nm comes from the scattered laser and from the X^+ state which is pumped via a phonon-assisted process. Reducing the defect density and/or the intentional doping may reduce this effect. Illumination with a weak above-band laser was not found to decrease the X^+ emission of this QD. The subsequent measurements shown in Fig. 31 were performed on the XX transition because it is expected to exhibit superior coherence properties compared to the X transition. To circumvent the low signal under pulsed excitation, CW measurements are performed. In Fig. 31(b) an HBT measurement of $g^{(2)}_{HBT}(\tau)$ is shown. Superimposed on the expected antibunching feature at zero time-delay, a strong bunching can be seen and it has to be taken into account when normalizing the data to the Poissonian level (see insets in Fig. 3 for long time delays). The best agreement between the data and a fit function is achieved when including three distinct processes leading to bunching. The fit function applied here reads

$$g^{(2)}_{HBT}(\tau) = a\left(1 - b\cdot exp\left(-\frac{|\tau-\tau_0|}{T_b}\right)\right) \times \prod_{i=1}^{3}\left(1 + c_i\cdot exp\left(-\frac{|\tau-\tau_0|}{T_{c,i}}\right)\right)$$

with a, b, c_i, $T_{c,i}$, and τ_0 as fitting parameters. The parameter T_b depends on the radiative lifetime and the pumping rate. The resulting time constants for the bunching are $T_{c,1}$ = (6.63 ± 2.0) ns, $T_{c,2}$ = (23.99 ± 2.2) ns and $T_{c,3}$ = (116.8 ± 27) ns. Possible reasons for this behavior are spectral diffusion due to background charge carriers, phonon-assisted laser re-excitation of the XX from the X, spin flips rendering a bright X in a dark state and vice versa, fluctuations of the local magnetic field due to nuclear spins, and/or background carriers randomly occupying the QD states, impeding the excitation of the XX. Bunching due to blinking is usually observed in RF. The fit according to the equation above gives $g^{(2)}_{HBT,\,raw}(0) = 0.102 \pm 0.109$. When the data are deconvoluted with the Gaussian-shaped system response function of the detectors and the electronics (FWHM = 93 ps measured via the

The EMPIR initiative is co-funded by the European Union's Horizon 2020 research and innovation programme and the EMPIR Participating States

autocorrelation of a picosecond laser pulse), a value of $g^{(2)}_{\mathrm{HBT,\,decon}}(0) = 0.072 \pm 0.104$ was obtained, confirming the high single-photon purity expected for TPE of a QD. The errors are calculated via error propagation from the 1σ-confidence bounds of the fitting parameters determined by the nonlinear least-squares-fitting algorithm. To evaluate the indistinguishability of the emitted XX photons in TPE, an unbalanced, fibre-based Mach–Zehnder interferometer with a delay line of 14.3 ns is used. To resolve the degree of the Hong-Ou-Mandel (HOM) effect expected for indistinguishable photons, the contrast between the autocorrelation measurement with co-polarized (indistinguishable) and cross-polarized (distinguishable) photons is evaluated. For this, the polarization of the photons can be changed independently in the two interferometer arms. The HOM visibility, i.e., the degree of indistinguishability, is then calculated as $V_{\mathrm{HOM}} = 1 - g^{(2)}_{\mathrm{parallel}}(0)/g^{(2)}_{\mathrm{perpendicular}}(0)$ from the zero-delay autocorrelation values of the indistinguishable and distinguishable cases. To fit the data, the conventional equation for HOM measurements with continuous wave excitation was used, inserting, however, equation above for $g^{(2)}_{\mathrm{HBT}}(\tau)$ to account for the bunching behaviour. As expected, the obtained bunching time scales are similar to the ones in the HBT measurement. Since the bunching behaviour differs slightly between the co- and cross-polarized measurement, the bunching constants c_i are set to zero within the evaluation, so as to exclude this as an error for the calculation of the visibility. Here, the normalized autocorrelation function is expected to drop to 0.5 for distinguishable photons and vanishing time delay. The measured value of $g^{(2)}_{\mathrm{HOM,perpendicular}}(\tau) = 0.463 \pm 0.097$ (0.471 ± 0.093 before the deconvolution) is in good agreement with this. The autocorrelation for indistinguishable photons yields $g^{(2)}_{\mathrm{HOM,parallel}}(\tau) = 0.049 \pm 0.04$ (0.135 ± 0.045 before the deconvolution). The maximal postselected degree of indistinguishability of the photons is calculated to be $V_{\mathrm{HOM,decon}} = 0.894 \pm 0.109$ ($V_{\mathrm{HOM,raw}} = 0.713 \pm 0.15$) including (excluding) the deconvolution of the data with the system response function. The width of the central dip is a measure of the temporal postselection window necessary for possible time-gated applications. The 1/e rise time is given by T_b, from which a full width of $2T_b$ = (1.156 ±0:14) ns is determined. Apart from approaches relying on quantum frequency conversion, this constitutes the first direct measurement of the mutual, postselected degree of indistinguishability of

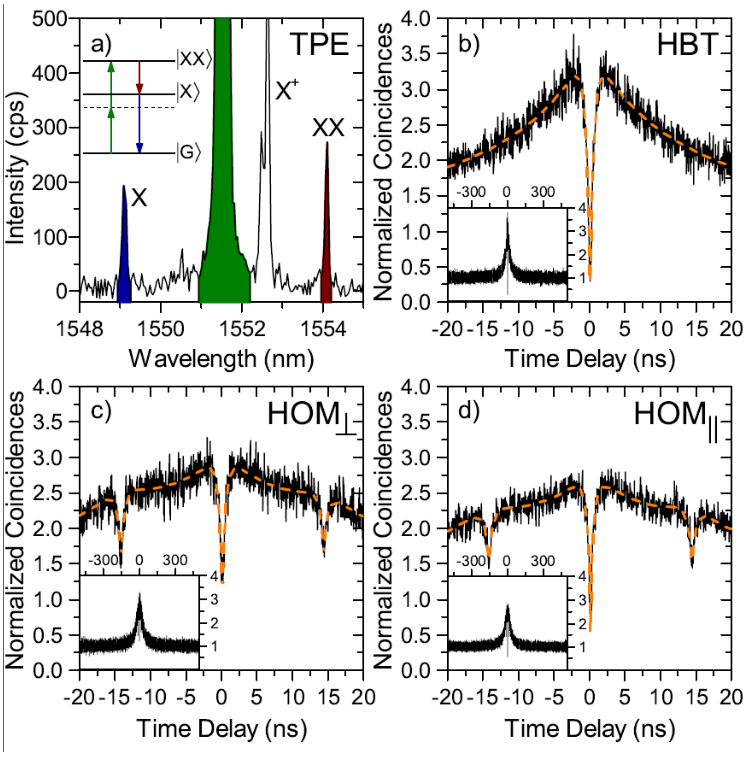

Figure 30. Two-photon excitation: (a) Spectrum and energy diagram. (b) Second order intensity autocorrelation measurement with the fit function (orange). (c) and (d) TPI of distinguishable and indistinguishable photons in TPE with respective fit functions (orange). The insets of (b)–(d) show the same data with a correlation window of ±500 ns. The measurements shown in (b)–(d) are performed with a count rate of ~16 kcps and an integration time of ~12 h. Figure and caption from [Nawrath2019].

QD photons in the telecom C-band, complementing the demonstration of the three basic prerequisites for quantum applications, namely, single-photon emission, entangled-photon pair emission, and indistinguishability. In conclusion, a study on the coherence of InAs/InGaAs/GaAs QDs emitting in the telecom C-band was presented. Fourier transform spectroscopy in AB pumping revealed a mean linewidth of 9.74 GHz for transitions from 9 exemplary QDs due to the very strong influence of inhomogeneous broadening effects, motivating the change to resonant pumping schemes. In RF, the mean linewidth of five QDs is reduced to 3.50 GHz. Furthermore, coherent state preparation with a fidelity of 49.2% in pulsed RF paves the way to on-demand generation of telecom C-band photons with good coherence. Offering the inherent possibility of polarization-entangled photon pair emission, TPE is investigated as another resonant excitation scheme. The autocorrelation function of the XX line exhibits bunching behaviour on three different time scales as is typically observed in resonant pumping schemes. Finally, the postselected degree of indistinguishability of the XX transition is determined under CW excitation. These results motivate further work on GaAs-based telecom C-band QDs to improve on the values for quantum optical properties achieved with state-of-the-art QDs.

Finally, a study on the single-photon purity and indistinguishability under pulsed quasi-resonant p-shell excitation and in pulsed resonance fluorescence of In(Ga)As QDs emitting in the telecom C-band was performed. The InAs QDs are grown on a linearly-graded MMB layer of 1080 nm thickness and capped by 220 nm of InGaAs, forming a weak 3-λ cavity between the semiconductor air interface and a DBR consisting of 20 AlAs/GaAs pairs. The sample was kept in a helium-flow cryostat at 4.5 K and excited optically. For p-shell excitation a cw laser chopped by an electro-optic modulator is used to generate pulses of ~ 100 ps, whereas the RF measurements are done with a mode-locked laser with a pulse length of 9 ps. In both cases the fluorescence signal is discriminated from the laser by a cross-polarized excitation/detection setup and later filtered to ~ 5 GHz. To evaluate the single-photon purity, the second-order autocorrelation function $g^{(2)}(\tau)$ is recorded in an HBT setup employing a fibre-based beam splitter. The results along with the respective fit functions are displayed in Fig. 32.

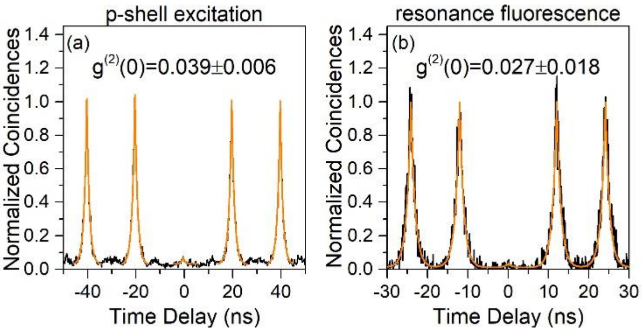

Figure 31. Second-order auto-correlation measurement under (a) pulsed p-shell excitation and (b) in pulsed resonance fluorescence including fit functions (orange).

Note that for the case of p-shell excitation, the measurement artefacts at correlation times other than multiples of the repetition time 20 ns are due to the non-ideal pulse generation, including secondary pulses. To distinguish this from residual multi-photon components at zero time-delay in the correlation measurement, the fit function excludes these artefacts. Both p-shell excitation and RF yield excellent single-photon purity values with $g^{(2)}(0)$ = 0.039 ± 0.006 and $g^{(2)}(0)$ = 0.027 ± 0.018, respectively, including background correction. To evaluate the indistinguishability of consecutively emitted photons in both excitation schemes, an unbalanced Mach-Zehnder interferometer with adjustable polarization in both arms is employed. The degree of two-photon interference (TPI), i.e. the degree of indistinguishability, is measured by comparing the correlation peak at zero time-delay between intentionally cross-polarized, i.e. perfectly distinguishable, and co-polarized photons.

Completely indistinguishable photons impinging in the second beam splitter of the MZI from two different input ports are expected to coalesce and therefore not result in a correlation event detected at zero time-delay. The results are displayed in Fig. 33.

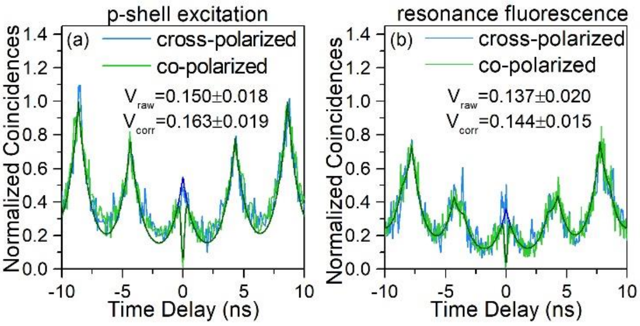

Figure 32. Two-photon interference measurements under (a) pulsed p-shell excitation and (b) in pulsed resonance fluorescence. Measurements and fit functions with cross-polarized photons are displayed in blue, whereas green stands for co-polarized photons.

Note also that in p-shell excitation, the repetition rate of the excitation is set to the delay of the unbalanced MZI of 4.319 ns, whereas in RF the excitation signal is sent into another unbalanced MZI to generate a double-pulse pattern with the respective time separation. For this reason, the correlation histogram for the RF case consists of a series of overlapping peaks. Both data sets are fitted with a model including spectral diffusion and based on the ratio of the areas of the central peak yield TPI visibility values of 0.163 ± 0.019 (0.150 ± 0.018) for p-shell exciation and 0.144 ± 0.015 (0.137 ± 0.020) in RF when correcting for all setup imperfections (only background emission), respectively. These values indicate substantial decoherence mechanisms on the time scale in question for both excitation schemes impacting the degree of indistinguishability. While the identification and mitigation of these processes is of crucial importance to increase the indistinguishability, these measurements represent the first demonstration of the determination of the TPI visibility under pulsed excitation of QDs emitting in the telecom C-band. Furthermore, the pronounced dip in the central peak offers the possibility for time-gated application of these photons. Using such post-selection schemes, a maximal value of 0.920 ± 0.0001 and 0.955 ± 0.0001 for p-shell excitation and RF is attained in this measurement, respectively. In conclusion, we compared p-shell excitation and RF in pulsed mode for QDs emitting directly in the telecom C-band, showing very high single-photon purity values and a proof-of- principle measurement of the degree of indistinguishability for both excitation schemes. An identification and reduction of decoherence mechanisms, is envisioned to transfer the high TPI visibility values measured under post-selection to schemes not relying on such techniques.

The EMPIR initiative is co-funded by the European Union's Horizon 2020 research and innovation programme and the EMPIR Participating States

Summary

Single molecules

Table 1 summarises the results of the investigations into optimising the coupling of single-photon emission from single-molecules into waveguides. Measurements of photon purity, i.e. $g^{(2)}(0)$, and indistinguishability for nanocrystals embedded in waveguides were not achievable within the project, but measurements performed on a system comprising a nanocrystal on top of a gold mirror on which a solid immersion lens was fabricated around the nanocrystal, yielded $g^{(2)}(0) = 0.00 \pm 0.03$ and indistinguishability ~ 0.8.

	Polymeric waveguide	Si_3N_4 on SiO_2 ridge waveguide	Si_3N_4 disk resonator	Polymeric ridge waveguide on top of Bragg mirror
Emitter-waveguide coupling efficiency	~ 10%	~ 10%	~ 78%	Not yet measured
Comment	Estimated from measurement data	Estimated from measurement data	Predicted from limited experimental data	Device designed within SIQUST

Table 1: Coupling efficiencies for various waveguide structures.

Quantum dots

Table 2 summarises the measurements obtained for the various excitation schemes studied in the three investigated systems. The monolithic structure, of necessity, could only be pumped at the emission wavelength of the integrated electrically-driven LED. The ‚standalone' quantum dot structures for 930 nm and 1550 nm emission could be excited at various wavelengths. $g^{(2)}(0) < 0.1$ was observed in all measurements. Two-photon resonant pumping yielded an entanglement fidelity of 0.8 for the optically pumped 930 nm quantum dots and an indistinguishability ~ 0.9 for the 1550 nm quantum dots.

SYSTEM	METRIC	Excitation			
		Non-resonant	Quasi-resonant	Resonant	Two-photon resonant
930 nm (laser pumped)	$g^{(2)}(0)$		(12 ± 2) %	(7.3 ± 0.5) %	~ 7%
	Entanglement fidelity				0.8
935 nm (LED pumped)	$g^{(2)}(0)$	< 10%			
1550 nm (laser pumped)	$g^{(2)}(0)$		(3.9 ± 0.6) %	(2.7 ± 1.8) %	(7.2 ± 10.4) %
	Indistinguishability		0.163 ± 0.019	0.144 ± 0.015	0.894 ± 0.109

Table 2: Measured parameters for different quantum dots systems as a function of excitation

Table of Figures

List of Tables

The EMPIR initiative is co-funded by the European Union's Horizon 2020 research and innovation programme and the EMPIR Participating States

Glossary

AC:	anthracene
BJT:	bipolar junction transistor
BSW:	Bloch surface waves
CW:	continuous wave
DBR:	dielectric Bragg reflector
DBT:	dibenzoterrylene
DBT:AC:	dibenzoterrylene in anthracene
DC:	direct current
DLW:	direct laser writing
EL:	electroluminescence
FDTD:	finite-difference time-domain
FWHM:	full-width at half-maximum
$g^{(2)}$:	second-order correlation function
HBT:	Hanbury Brown & Twiss
HOM:	Hong-Ou-Mandel
LED:	light-emitting diode
MMB:	metamorphic buffer
MZI:	Mach-Zehnder interferometer
NC:	nanocrystal
NIR:	near-infrared
PVA:	polyvinyl alcohol
QD:	quantum dot
QW:	quantum well
RF:	resonant fluorescence
RT:	room temperature
SEM:	scanning electron microscopy
SPAD:	single-photon avalanche diode
SPS:	single-photon source
TPE:	two-photon excitation
TPI:	two-photon interference
TCSPC:	time-correlated single-photon counting
SPS:	single-photon source
WG:	waveguide

EMPIR EURAMET
The EMPIR initiative is co-funded by the European Union's Horizon 2020 research and innovation programme and the EMPIR Participating States

References

Section 1 - Single molecules

[Pazzagli2018] S. Pazzagli et al., “Self-Assembled Nanocrystals of Polycyclic Aromatic Hydrocarbons Show Photostable Single-Photon Emission”, *ACS Nano* 12 (5), 4295-4303 (2018)

[Perani2020] T. Perani and M. Liscidini, “Long-range Bloch surface waves in photonic crystal ridges”, *Optics Lett.* 45 (23), 6534 (2020)

[Colautti2020] M. Colautti et al., “A 3D Polymeric Platform for Photonic Quantum Technologies”, Adv. Quantum Technol. 3, 2000004 (2020)

[Ciancico2019] C. Ciancico et al., “Narrow Line Width Quantum Emitters in an Electron-Beam-Shaped Polymer”, *ACS Photonics* 6, 3120-3125 (2019)

[Lombardi2021] P. Lombardi et al., ”Triggered emission of indistinguishable photons from an organic dye molecule”, *Appl. Phys. Lett.* 118 (20), 204002 (2021)

Section 2.1 - NIR (930 nm region) optically-pumped devices [TUB]

[Bounouar2018] S. Bounouar et al., “Generation of maximally entangled states and coherent control in quantum dot microlenses”, *Appl. Phys. Lett.* 112, 153107 (2018)

Section 2.2 - NIR (930 nm region) electrically-driven devices [CSIC]

[Yuan2002] Z. Yuan et al., “Electrically Driven Single-Photon Source“, *Science* 295, 102 (2002)

[Alen2018] B. Alén et al. “Monolithic Quantum Light Source with Hybrid Pumping”, SPIE Optics and Photonics, San Diego - USA 20/08/2018

[Alen2019a] B. Alén et al “Device for emitting single photons or entangled photon pairs”. European Patent EP 3 361 516 B1 (published 18/12/2019)

[Alen 2019b] B. Alén et al.“Development of a plug & play single photon source using electro-optical pumping schemes”, Single Photon Workshop Milán - Italy 21/10/2019

[Alen2020] B. Alén et al. “Electrically driven and tunable plug & play single photon sources” Invitada. 3rd International Symposium on Single Photon based Quantum Technologies. Berlin - Germany 15/09/2020

Section 2.3 - Telecom wavelength (1550 nm region) implementation [USTUTT]

[Nawrath2019] C. Nawrath et al., “Coherence and indistinguishability of highly pure single photons from non-resonantly and resonantly excited telecom C-band quantum dots”, *Appl. Phys. Lett.* 115, 023103 (2019).

[Nawrath2021] C. Nawrath et al., “Resonance fluorescence of single In(Ga)As quantum dots emitting in the telecom C-band”, *Appl. Phys. Lett.* 118, 244002 (2021).